



# eBRAIN-Health

## Public report

## Dynamic principles of aging and neurodegeneration simulation demonstrator

Project number	<b>101058516</b>
Project title	<b>eBRAIN-Health - Actionable Multilevel Health Data</b>
Submission date	<b>March 2024</b>
Authors	<b>UPF</b>
Dissemination level	<b>Public (PU)</b>
Public project website	<b><a href="https://ebrain-health.eu/">https://ebrain-health.eu/</a></b>



## Table of content

1. eBRAIN-Health .....	3
2. Introduction .....	3
3. Partners involved .....	3
4. Description of work performed .....	3
4.1. INSIDEOUT framework.....	4
4.2. Non-equilibrium Framework.....	6
4.3. Intrinsic ignition Framework .....	7
4.4. Neuroimaging data .....	8
4.4.1. Aging .....	8
4.4.2. Alzheimer .....	9
5. Results.....	10
5.1. INSIDEOUT framework in aging .....	10
5.2. Non-equilibrium framework in Alzheimer’s disease.....	11
5.3. Intrinsic ignition framework in Alzheimer’s disease .....	11
6. Conclusion, next steps .....	13
7. Figures and Tables .....	14
8. Bibliography .....	21

## 1. eBRAIN-Health

The Project eBRAIN-Health will deliver a distributed research platform for modeling and simulating complex neurobiological phenomena of human brain function and dysfunction in a data protection compliant environment. It will provide thousands of multilevel virtual brains from patients and healthy human controls for research and innovation. Brain data from multiple sources will be pre-processed. Solving the societal grand challenge of dementia is a big task. Yet it appears feasible in a collective approach. Therefore, we will build an interdisciplinary digital twin for dementia for modeling and simulating complex phenomena at the service of research infrastructure communities. eBRAIN-Health-Cloud will offer end-to-end services for personalized complex brain modeling and simulations in distributed e-infrastructures with data protection by design and by default and simulation-ready human multiscale brain data that range from molecular (genomics, proteomics, metabolomics) and cellular to electrophysiology and imaging to behavioural, clinical, life-style and environmental data as well as data from wearables. Brain data are pre-processed and annotated such that they all relate to a common reference 3D brain space.

eBRAIN-Health-Cloud constitutes a blend of three large-scale research programs: the FET Flagship Human Brain Project with its EBRAINS Research Infrastructure, the EOSC project Virtual Brain Cloud with its Virtual Research Environment for sensitive data and the H2020 project AI-MIND with intelligent tools for dementia risk estimation. The project will have synergies to topics of the Digital Europe Program, such as artificial intelligence, cybersecurity and supercomputing and the Health Data Space.

eBRAIN-Health-Cloud offers a next generation clinical research infrastructure and creates an open yet protected space for groundbreaking digital health innovation by the research infrastructure communities comprising academia and the private sector.

## 2. Introduction

Our research aims better to understand brain dynamics in normal aging and neurodegeneration. We use neuroimaging techniques and theoretical frameworks to explore brain network organization and function across different demographic groups and brain states.

Our work focuses on developing and extending three theoretical frameworks: the INSIDEOUT (Deco et al., 2022), Non-equilibrium (In prep.), and Intrinsic Ignition frameworks (Deco et al., 2017). Here, these frameworks have proven effective in investigating the dynamic mechanisms responsible for age-related changes and neurodegenerative processes.

This deliverable report presents comprehensive analyses of brain network dynamics in aging and the progression of Alzheimer's disease. Our findings reveal significant differences in irreversibility measures, equilibrium deviations, and node-metastability alterations, indicating differences in brain network organization in aging, sex, and the progression of Alzheimer's disease.

## 3. Partners involved

UPF, IBEC, CHARITE

## 4. Description of work performed

Our primary aim is to gain a deeper understanding of the underlying brain dynamic mechanisms underlying the aging process and neurodegeneration. To achieve this, we have developed and evaluated three theoretical approaches across two distinct neuroimaging datasets (one focused on aging and the other on Alzheimer's disease). Specifically, we have tested the INSIDEOUT framework in the aging neuroimaging dataset and evaluated both the Non-equilibrium and Intrinsic Ignition Frameworks in the Alzheimer's neuroimaging dataset.

In this section, we provide detailed explanations of the methodologies developed and descriptions of the neuroimaging datasets employed.

#### 4.1. INSIDEOUT framework

We have developed a novel approach that identifies the balance between intrinsic and extrinsic dynamics in brain states, providing insights into the non-equilibrium nature of brain dynamics. Inspired by thermodynamics, this framework uses the arrow of time to discern the level of non-reversibility (or irreversibility) and asymmetry in the temporal processing, thereby capturing the non-equilibrium dynamics of the brain. This framework has revealed significantly different signatures of irreversibility in different brain states, such as deep sleep, anesthesia (Deco et al., 2022), disorders of consciousness (Guzmán et al., 2023), and neurodegeneration (Cruzart et al., 2023), offering a novel tool for studying the balance of intrinsic and extrinsic dynamics in different brain states.

Computing the level of irreversibility relies on detecting the arrow of time through the degree of asymmetry obtained by comparing the causal relationship between pairwise time series of the forward and the artificially generated time-reversed version. Specifically, we consider first the detection of the level of non-equilibrium (i.e. the arrow of time) between two time series  $x(t)$  and  $y(t)$ , where  $x(t)$  is evolving from an initial state  $A1$  to a final state  $A2$ , and  $y(t)$  is evolving from an initial state  $B1$  to a final state  $B2$ , respectively. The time-reversed version of  $x^{(r)}(t)$  (or  $y^{(r)}(t)$ ), that we call  $x^{(r)}(t)$  (or  $y^{(r)}(t)$ ), is obtained by flipping the time ordering, (i.e., ordering the time evolution of  $x^{(r)}(t)$  (or  $y^{(r)}(t)$ ) as the inverted sequence determined by initial state  $A2$  to a final state  $A1$  (or initial state  $B2$  to a final state  $B1$ ). The time-shifted Pearson's correlation measures the causal dependency between the original time series  $x(t)$  and  $y(t)$ . For the forward evolution, the time-shifted correlation is given by

$$c_{forward}(\Delta t) = \langle x(t), y(t + \Delta t) \rangle$$

for the reversed backward evolution, the time-shifted correlation is given by the pairwise level of irreversibility, i.e., the degree of temporal asymmetry

$$c_{reversed}(\Delta t) = \langle x^{(r)}(t), y^{(r)}(t + \Delta t) \rangle$$

capturing the arrow of time is given consequently by the absolute difference between the causal relationship between these two-time series in the forward and reversed backward evolution at a given shift  $\Delta t = T$ , i.e.,

$$I_{x,y}(T) = |c_{forward}(T) - c_{reversed}(T)|$$

We keep the correlations with their signs and compute the absolute difference as we are interested in the magnitude of the change in the asymmetry. After computing the autocorrelation for all regions, subjects, and conditions, and observed that a sufficient decay occurs when  $T=1$ . This value,  $T$ , reflects the temporal domain where we assess our results; adjusting this parameter will allow us to find different results at different timescales. This  $T$  represents the time points shifted, of the discretized signal, meaning that the real-time association will depend on the time resolution of the acquired data.

The level of non-reversibility/non-equilibrium for the multidimensional case of whole-brain analysis can be easily generalized by defining the forward and reversal matrices of time-shifted correlations. The forward version of a multidimensional time series  $x_i(t)$  reflects the dynamical evolution of the variable describing the system. The sub-index,  $i$ , indicates the distinct dimensions of the dynamical system and  $x_i^{(r)}(t)$  denotes the corresponding reversed backward version. The forward and reversal matrices expressing the functional causal dependencies between the different variables for the forward and artificially generated reversed backward version of a multidimensional system are given by

$$FS_{forward,ij}(\Delta t) = -\frac{1}{2} \log(1 - \langle x_i(t), x_j(t + \Delta t) \rangle^2)$$

$$FS_{reversal,ij}(\Delta t) = -\frac{1}{2} \log(1 - \langle x_i^{(r)}(t), x_j^{(r)}(t + \Delta t) \rangle^2)$$

The  $FS$  functional causal dependencies matrices are expressed as the mutual information based on the respective time-shifted correlations. The level of irreversibility is given by the quadratic distance between the forward and reversal time-shifted matrices at a given shift  $\Delta t = T$ . In other words, the level of non-reversibility/non-equilibrium in the multidimensional case is given by

$$I = \| FS_{forward}(T) - FS_{reversal}(T) \|_2$$

where the notation  $\|Q\|_2$  is defined as the mean value of the absolute squares of the elements of the matrix  $Q$ . In other words, if we define a difference matrix  $FS_{reversibility}$  as

$$FS_{reversibility,ij} = (FS_{forward,ij}(T) - FS_{reversal,ij}(T))^2$$

the matrix  $FS_{reversibility}$  is thus a matrix whose elements are the squared of the elements of the matrix  $(FS_{forward}(T) - FS_{reversal}(T))$  where for each pair, the level of irreversibility is measured by the squared difference. Thus,  $I$  is simply the mean value of the elements of  $FS_{reversibility}$ . In summary, we reduce the mutual information ( $FS$ ), forward and reverse cases, based on the respective time-shifted ( $T$ ) correlations into a single value corresponding to the mean of the  $FS_{reversibility}$  matrix that defines the degree of asymmetry of the time series. However, this process could be done iteratively by dividing the time series into a subset of time points, i.e. a sliding window of length  $W$ , resulting in a dynamic characterization of the asymmetry within a subject. Every sliding window ( $W$ ) is described by the mean of its corresponding  $FS_{reversibility}$  matrix. For instance, every subject is described by a set of  $N$  reversibility

values (mean of  $FS_{reversibility}$  matrix) being  $N$  the number of total sliding windows, depending on the length of the timeseries and the window size ( $W$ ). We computed the  $FS_{reversibility}$  over all participants and all sliding windows for each condition. For the global level of asymmetry, we computed for each sliding window the degree of asymmetry as the mean value of the elements of the  $FS_{reversibility}$  matrix. Each subject is characterized as the average reversibility values and their standard deviation, later on called deviation reversibility.

## 4.2. Non-equilibrium Framework

### Deviation from Equilibrium Formalism

In physics, one of the possibilities to study the deviations from equilibrium is using thermodynamics, particularly the Fluctuation Dissipation Theorem formalism. A way of expressing the deviations from equilibrium within this formalism is through the relation between the linear response function and the auto-correlation function. The linear response function of an observable  $x$  of the system to a small enough perturbation  $h$  is given by:

$$x(t) = \int_{t'}^t R(t, t') h(t') dt'$$

where  $h(t)$  is the perturbation that must be small. Independently, the auto-correlation (or two-point correlation function) is defined as

$$C(t, t') = \langle x(t)x(t') \rangle$$

where here  $\langle . . . \rangle$  stands for the average over a sufficiently large set of realizations of the object of study (i.e., an ensemble average). The formulation we are using here of the theorem states that for a system in equilibrium, the linear response function  $R$  is related to the auto-correlation of the unperturbed observable  $x$  by

$$R(t, t') = \beta \frac{\partial C(t, t')}{\partial t'}$$

for  $t' \leq t$  and the variable  $\beta$  being identified with the inverse of the thermal bath temperature  $1/T$ . For out-of-equilibrium systems, this expression is not valid and must be rewritten as:

$$R(t, t') = \beta X(t, t') \frac{\partial C(t, t')}{\partial t'}$$

The function  $X(t, t')$  is called the Fluctuation-Dissipation Ratio and characterizes the approach to equilibrium and measures the deviation from FDT. Also, a way to measure the separation from FDT, and therefore from equilibrium, is through the Integral Violation  $I(t, t')$  of FDT given by

$$I(t, t') = C(t, t) - C(t, t') - T \chi(t, t')$$

Where  $\chi(t, t') \equiv \int_t^t R(t, t') ds$  is the integrated response function, or dynamic susceptibility. For systems in equilibrium, we recover the original expressions by setting  $\chi = 1$ ,  $V = 0$ , and  $I = 0$ . Now, in the case of the system evolves with a Langevin equation

$$\frac{dx}{dt} = -F[x](t) + \eta(t)$$

where  $F$  is a deterministic function and  $\eta(t)$  is a zero-mean Gaussian noise with auto-correlation  $\langle \eta(t)\eta(t') \rangle = 2T\delta(t - t')$ , we can reformulate the above expressions and get

$$R(t, t') = \frac{1}{2T} \langle x(t)\eta(t') \rangle$$

we can also define the asymmetry  $A$  as:

$$A(t, t') \equiv \langle F[x](t) x(t') \rangle - \langle F[x](t') x(t) \rangle$$

The degree of non-equilibrium could be used as a marker of brain disease states.

#### Model-free Derivation

We define our observable  $x(t)$  as being the BOLD signal of a given brain region. In that case, we can try to impose the Langevin equation we introduced in Equation 1 and develop the formalism presented in the previous section. The first step, to numerically compute its derivative  $dx/dt$ , is easy, so the only problem we face is how to split the signal into its two components, the unknown operator  $F[x](t)$  and the noise  $\eta(t)$ . The key idea we use to develop the ideas further is to split the  $dx/dt$  signal into two components: first, we filter it by applying a Wiener filter, and we call the result  $-F[x](t)$  (observe the negative sign). Second, we obtain  $\eta(t)$  by simply adding the unfiltered and filtered versions of the signal:

$$\eta(t) = \frac{dx}{dt} + F[x](t)$$

However,  $\eta(t)$  cannot be any kind of function, it must satisfy two key requirements: being Gaussian, and

$$\langle \eta(t)\eta(t') \rangle = 2T\delta(t - t')$$

which we informally call the sanity check of the noise signal  $\eta(t)$ . If the signal satisfies these conditions, we can proceed with the rest of the equilibrium analysis

### 4.3. Intrinsic Ignition Framework

Metastability in brain dynamics refers to a state in which the brain's activity displays persistent deviations from its natural equilibrium state. This state allows the brain to exhibit both autonomous and coordinated tendencies, enabling the emergence of dynamic patterns of interaction among distributed neural ensembles.

The Intrinsic Ignition Framework allows to evaluate the effect of intrinsic local perturbations (i.e., neural events), reflecting the capacity of a brain area to propagate neural activity to other brain areas.

The evaluation of each area's node-metastability is measured as the standard deviation of integration over time. In other words, this framework quantifies the degree of whole-brain integration from spontaneously occurring events over time. In particular, this algorithm captures driving events for each brain area, which are transformed into a binary signal using a threshold method. To represent events as a binary signal, time series are transformed into z-scores, denoted as  $z_i(t)$ , and a threshold value,  $\theta$ , is applied. Specifically, an event is marked as 1 in the binary sequence  $\sigma(t)$  if  $z_i(t)$  exceeds the threshold from below and marked as 0 otherwise. When a brain area triggers an event, neural activity is measured in all brain areas within a set time window of  $4TR$ . A binary matrix is then constructed to represent the connectivity between brain areas exhibiting simultaneous activity. The measure of global integration is applied to determine the broadness of communication across the network for each driving event (i.e., the largest subcomponent). This process is repeated for each spontaneous neural event to obtain the node-metastability (measured as the standard deviation of the integration over time) for each brain area across the network, where higher node-metastability corresponds to higher dynamical complexity. Thus, each brain area can be classified according to its local degree of functional variability, i.e., local- or node-metastability. In other words, different levels of temporal diversity in a given brain area can be considered a measure of local functional variability or metastability and thus describe the versatility of a given area within the network. This analysis can be assessed across the whole brain and within specific resting-state networks for each subject.

#### 4.4. Neuroimaging data

##### 4.4.1. Aging

###### Participants

A total of 723 healthy subjects aged 50 years or older were included (Puig et al., 2020, Escrichs et al., 2023). We established the cutoff age between groups based on the definition of “elderly” people as those aged  $> 65$ . See Table 1: Aging. Demographic characteristics of participants.

###### MRI data acquisition

MRI images were acquired using a mobile 1.5 T scanner (initially from Toshiba Medical Systems and now from Canon Medical Systems). An 8-channel phased-array head coil with foam padding was used to restrict head movement, along with noise-canceling headphones. The acquisition included a high-resolution axial T1-weighted sequence and a gradient echo-planar imaging (EPI) sequence with 122 functional volumes acquired during resting-state fMRI. The details of the acquisition parameters are as follows: 112 slices were obtained for the T1-weighted sequence, with a repetition time (TR) of 8 ms, echo time (TE) of 4.5 ms, flip angle of  $15^\circ$ , field of view (FOV) of  $235 \times 235$  mm, and voxel size of  $1.3 \times 1.3 \times 2.5$  mm. For the EPI sequence: TR = 2500 ms, TE = 40 ms, flip angle =  $83^\circ$ , FOV =  $230 \times 230$  mm, and voxel size =  $3.5 \times 3.5 \times 5$  mm without a gap. Participants were instructed to relax, remain motionless, remain awake, and keep their eyes closed to minimize stimuli, including visuals.

###### Preprocessing

T1 and EPI images were oriented automatically using Conn (Whitfield., 2012). We utilized the Data Processing Assistant for Resting-State fMRI (DPARSF) toolbox based on Statistical Parametric Mapping (SPM12) (Chao et al., 2010). The following steps were taken: 1) discarding the first five volumes to allow for signal stabilization, 2) correcting for slice-timing, 3) realigning to correct head motion across different volumes, 4) co-registering the functional image to the T1-weighted image, 5) normalizing by using T1 image unified segmentation, 6) regressing nuisance covariates, which included six parameters

from the head motion correction, white matter and the cerebrospinal fluid signal using CompCor, 7) removing the linear trend in the time series, 8) spatially normalizing to the MNI standard space, 9) smoothing spatially with a 6-mm full-width at half-maximum Gaussian kernel, and 10) band-pass filtering temporally (0.01–0.09 Hz).

#### 4.4.2. Alzheimer

##### Participants

We used the ADNI database to gather 17 healthy controls (HC), 9 mild cognitive impairment (MCI) patients, and 10 patients with Alzheimer’s Disease (AD) from ADNI (Stefanovski et al., 2019, Triebkorn et al., 2022). See Table 2: Alzheimer. Epidemiological information of the population. Given these cohorts, we used the G\*Power software to conduct statistical power calculations based on a two-group Wilcoxon-Mann-Whitney test, with significance level  $\alpha = 0.05$  and power  $1 - \beta = 0.8$ . Assuming a standard deviation  $\sigma = 0.05$  (a reasonable assumption given our results below), we obtained that the minimum effect size we would be able to discern in this setting would be  $d = 1.1$ , which implies that the minimum detectable difference between the means of the control population and any of the other two would be around 0.055.

##### MRI data acquisition

Images were downloaded from ADNI-3, which used data from Siemens scan. As this data is the same as previously reported, we will limit its description to an abridged processing version. The following imaging modalities were included: T1 MPRAGE. TE = 2.95– 2.98ms, TR = 2.3 s, matrix and voxel size differ slightly. FLAIR. TE differs slightly, TR= 4.8 s, matrix size =  $160 \times 256 \times 256$ , and voxel size differs slightly. DWI (only for 15 HC participants to create an average healthy SC). TE = 56–71ms, TR =3.4–7.2 s, matrix size =  $116 \times 116 \times 80$ , voxel size =  $2 \times 2 \times 2$ , bvals = [0, 1000] or [0, 500, 1000, 2000], bvecs = 49 or 115. Siemens Fieldmaps and PET Data (AV-45 for Abeta). The preprocessing of imaging data can be subdivided into structural images, DWI, and PET.

##### Preprocessing

The pre-processing of resting-state fMRI was computed using FSL FEAT and independent component analysis–based denoising (FSLFIX) following a standard pipeline (Stefanovski et al., 2019), which included removal of the first four volumes, rigid-body head motion correction, 3-mm spatial smoothing to improve signal-to-noise ratio, and a high-pass temporal filter of 75 s to remove slow drifts. The data were then denoised using FSLFIX, an independent component analysis–based denoising method that uses an automated classifier to identify noise-related components for removal from the data. The algorithm was trained on a manually labeled held-out set of 25 individuals scanned with identical imaging parameters. Time courses for noise-labeled components and 24 head motion parameters were then removed from the voxel-wise fMRI time series using ordinary least squares regression.

The resulting denoised functional data were spatially normalized to the International Consortium for Brain Mapping 152 template in Montreal Neurological Institute (MNI) space using Advanced Normalization Tools (version 2.2.0) via a three-step method: (I) registration of the mean realigned functional scan to the skull-stripped high-resolution anatomical scan via rigid-body registration; (II) spatial normalization of the anatomical scan to the MNI template via a nonlinear registration; and (iii) normalization of the functional scan to the MNI template using a single transformation matrix that concatenates the transforms generated in steps I and II. Mean time series for each parcellated region

were then extracted, and interregional FC matrices were estimated using Pearson correlations between each pair of regional time series. Dynamic FC matrices were also calculated for the empirical data, as outlined below.

## 5. Results

The following is a breakdown of the outcomes achieved for each theoretical framework. Section 5.1 explains the INSIDEOUT framework's results when applied to the aging dataset. Section 5.2 describes the results of the Non-equilibrium framework when applied to the Alzheimer's dataset. Finally, section 5.3 describes the results of the Intrinsic ignition framework when applied to the Alzheimer's dataset.

### 5.1. INSIDEOUT framework in aging

First, we computed the irreversibility measure across the whole-brain network. We found significant differences in irreversibility among age groups and sex. In particular, we observed that older males exhibited a higher degree of irreversibility compared to older females ( $p=0.0236$ ), indicating an association between age, sex, and brain network dynamics. Additionally, middle-aged males showed a higher degree of irreversibility compared to middle-aged females ( $p=0.01826$ ), emphasizing the complex interplay between age, sex, and brain network dynamics.

Second, our analysis of the irreversibility measure across resting-state networks revealed significant differences related to aging and sex (Figure 1). Specifically, within the medial frontal network (MDFT), significant differences in irreversibility were observed between female older and female middle-aged participants ( $p=0.04651$ ) and between female middle-aged and male middle-aged participants ( $p=0.02818$ ), highlighting age and sex-related variations in network dynamics. In the frontoparietal network, males exhibited higher irreversibility compared to females across different age groups ( $p=0.002517$  for male older vs. female older;  $p=0.03374$  for female middle-aged vs. male middle-aged), suggesting sex-specific differences in frontoparietal network organization. Within the default mode network (DMN), older male participants showed higher irreversibility compared to both male middle-aged ( $p=0.01975$ ) and older female participants ( $p=0.02984$ ), indicating age-related variations in network dynamics. Similarly, older males exhibited higher irreversibility in the subcortical network compared to older females ( $p=0.03145$ ), highlighting sex-related differences in subcortical network organization. In the motor network, males showed higher irreversibility compared to females across different age groups ( $p=0.001847$  for male older vs. female older;  $p=0.001704$  for female middle-aged vs. male middle-aged), suggesting robust sex differences in motor network organization. In the visual I network (VI), significant differences were observed between male middle-aged and female middle-aged participants ( $p=0.01186$ ), while older females showed higher irreversibility than middle-aged females ( $p=0.0148$ ). In the visual II network (VII), middle-aged male participants showed higher irreversibility than female middle-aged participants ( $p=0.003574$ ). Finally, in the visual association network (VASO), males exhibited higher irreversibility compared to females across different age groups ( $p=0.008519$  for males older vs. females older;  $p=0.03652$  for females middle-aged vs. males middle-aged), highlighting sex-specific variations in visual network dynamics.

Our findings highlight the significance of demographic factors in brain network organization in sex and aging studies. Further investigations are warranted to determine the underlying mechanisms driving these differences and their implications for cognitive function and brain health across the lifespan.

## 5.2. Non-equilibrium framework in Alzheimer's disease

The whole approach assumes that the residual noise  $\eta(t)$  satisfies both conditions: the Gaussianity test ( $\eta(t)$  must follow a Gaussian probability distribution) and the sanity check described above. To check the first part, we exhaustively checked the resulting noise signal with several different tests, including both visual (building a histogram and comparing it with a perfect Gaussian curve and a Q-Q plot) and analytical ones (Shapiro-Wilk's test, D'Agostino's K2 test, and Anderson-Darling's test). See Figure 2A. In the Shapiro-Wilk test, 92.69% of the tests returned a positive (Gaussian) result, and for D'Agostino's K2 test, the number of positive results was 91.65%. In the case of the Anderson-Darling test, critical values provided for the normal are for the following significance levels: 15%, 10%, 5%, 2.5%, 1%, giving the following results: 15.0: 84.56%; 10.0: 49.03%; 5.0: 95.00%; 2.5: 97.39%; 1.0: 98.82%. As we can see, our analysis yielded that, in general, the vast majority of the regions have a residual noise  $\eta(t)$  that satisfies the Gaussianity test. Concerning the sanity check, we used Equation 3 to verify that the noise signals  $\eta(t)$  are adequate for our purposes, rendering the whole approach useful for neuroscience applications. We have run numerical and visual inspections, as seen in Figure 2A (right panel), to check the diagonal, i.e., for  $t = t'$ , Dirac delta behavior. This requirement is widely satisfied in all the tested cases, both at the subject and the node levels. At Figure 2B we can observe that this framework allows a clean discrimination among the three cohorts, and at Figure 2C we can see renders of the subject-based average of the node-level deviation from equilibrium coefficients. We discern a pronounced deviation particularly evident within the HC cohort, gradually diminishing as the disease progresses through the MCI and AD stages. The results, outlined in Figure 3, highlight minimal deviations from equilibrium within the Limbic network across disease progression. Notably, during the initial stages—HC and MCI—no substantial alterations are observed within the default, salience, and control networks, contrasting with significant deviations evident between MCI and AD stages. Conversely, the visual network stabilizes values during the final stage. Furthermore, the dorsal attention and somatomotor networks exhibit significant variations in equilibrium values from the outset, positioning them as promising biomarker targets for patient diagnosis.

## 5.3. Intrinsic ignition framework in Alzheimer's disease

We measured the dynamical complexity underlying the whole-brain network in the three groups, i.e., HC, MCI, and AD. We found that the node-metastability significantly decreased in the AD group compared to the MCI ( $p < 0.001$ ) and HC ( $p < 0.001$ ). Furthermore, we found that the node-metastability was higher in MCI than in AD ( $p < 0.001$ ).

Figure 4A shows that the whole-brain dynamical complexity systematically decreases as the disease progresses, which is to be expected as the different regions have their dynamics altered.

Figure 4B shows the hierarchy for each disease stage across the whole-brain functional network (i.e., the sorted brain areas from highest to lowest node-metastability). The red shadow area represents the 10% brain areas showing the highest node-metastability values for each group. These regions correspond mainly to the visual network, closely followed by regions in the somatomotor and dorsal networks, although they show a systematic decrease as the disease progresses along its known stages.

Figure 4 we show the rendered brains representing the node-metastability for each group across the whole-brain functional network. Healthy controls show the highest metastability values compared to MCI and AD stages (FDR-corrected,  $p < 0.001$ ).

#### Node-metastability Across Resting State Networks

We assessed the node-metastability within each network to test group differences across resting-state networks, i.e., control, limbic, somatomotor, salience, DMN, and dorsal. Differences between groups for each network are depicted in Figure 5A. Compared to healthy controls, the MCI group presented a significant decrease in node-metastability across all resting state networks (FDR-corrected,  $p < 0.001$ ) except in the visual network, which remained almost unchanged (FDR-corrected,  $p > 0.05$ ). Furthermore, the AD group showed a significant decrease in node-metastability across all resting-state networks compared to healthy controls (FDR-corrected,  $p < 0.001$ ). Similarly, when compared to MCI, the AD group displayed a node-metastability decline in all networks, i.e., the control, somatomotor, salience, DMN, and dorsal (FDR-corrected,  $p < 0.001$ ) and limbic (FDR-corrected,  $p < 0.05$ ). Figure 5B shows a radar plot illustrating each group's average metastability values for each resting-state network.

#### Multilevel Modeling of AD on whole-brain and resting-state networks

We used mixed effects models for the whole brain to study the effect of both burdens, ABeta and tau, on the observed metastability. In this study, the metastability for each node was defined as the outcome variable, while, as explanatory variables, we used the ABeta and tau SUVR values for each region, and the patient ID as a random effect. As a parallel of the research done in this paper, we studied two different models, the first one adding the MMSE cohort each patient belongs to (i.e., HC, MCI, or AD) as fixed effects, to understand the effect of both misfolded proteins on the whole brain; and the second one including the RSN of each node, to understand their impact on the different networks.

#### Mixed effects models for the whole brain network.

We assessed whether the outcome variable (i.e., each node's metastability) shows a significant change by specifying the node ABeta and tau levels, as well as their interaction, as fixed effects, regardless of any other variable of the study. The interaction between cohort (i.e., disease progression) and amyloid and tau status was added as a fixed effect to the above models to assess whether change over time is differentially affected by ABeta and tau accumulation.

In general, we see that all stages show some dependency on the amount of tau present, with a clear increase of tau influence from healthy controls (Estimate =  $-1.106e-02$ , Std. Error =  $4.221e-03$ ,  $p = 0.008813$  \*\*), to MCI (Estimate =  $-5.723e-03$ , Std. Error =  $1.840e-03$ ,  $p = 0.001868$  \*\*) and AD patients (Estimate =  $3.224e-03$ , Std. Error =  $8.924e-04$ ,  $p = 0.000305$  \*\*\*), while increasing its statistical significance at the same time.

We can also appreciate that the effect of ABeta in the AD stage (Estimate =  $2.274e-03$ , Std. Error =  $1.033e-03$ ,  $p = 0.027768$  \*) is significant, as well as the interaction between both proteins at this stage (Estimate =  $-8.766e-04$ , Std. Error =  $2.983e-04$ ,  $p = 0.003303$  \*\*), which becomes quite significant.

See Figure 6. Multilevel models of the effects of ABeta and Tau on the whole brain.

Mixed effects models for resting-state networks. We assessed the RSN for each node. At this stage, we did not consider the disease stage, as adding it resulted in a more complex model without any significant improvement in its prediction power, as measured with pairwise ANOVA tests. Here, we

can appreciate that the role of tau is significant for both the DorsAttn network (Estimate =  $6.242e-03$ , Std. Error =  $2.339e-03$ ,  $p = 0.00819$  \*\*) and the SomMot network (Estimate =  $7.007e-03$ , Std. Error =  $3.519e-03$ ,  $p = 0.04699$  \*). We also see that the ABeta-tau interaction terms have a direct impact mainly on DorsAttn (Estimate =  $-1.978e-03$ , Std. Error =  $7.970e-04$ ,  $p = 0.01348$  \*), showing the synergistic effect of both burdens on the disease evolution. Figure 7: Multilevel models of the effects of ABeta and Tau on resting-state networks.

## 6. Conclusion, next steps

We developed, extended, and applied three theoretical frameworks across distinct neuroimaging datasets focused on aging and Alzheimer's disease.

Our investigation of brain dynamic mechanisms underlying normal aging shows differences between age and sex on temporal irreversibility of brain dynamics. We will extend our results by studying the effective connectivity and implementing classification Support Vector Machines (SVM).

Furthermore, our frameworks applied to the Alzheimer's data revealed patterns of equilibrium deviations and node-metastability alterations across the whole-brain and resting-state networks. We are currently preparing two manuscripts, one for the Non-equilibrium framework applied to Alzheimer's disease and the other for the Intrinsic Ignition framework in Alzheimer's.

Software:

The code for the INSIDEOUT framework applied to the aging neuroimaging dataset is publicly available on [https://github.com/aescrichs/aging\\_irreversibility](https://github.com/aescrichs/aging_irreversibility)

Upon acceptance of the articles, the code for the frameworks will also be openly accessible on GitHub and eBRAINS.

## 7. Figures and Tables

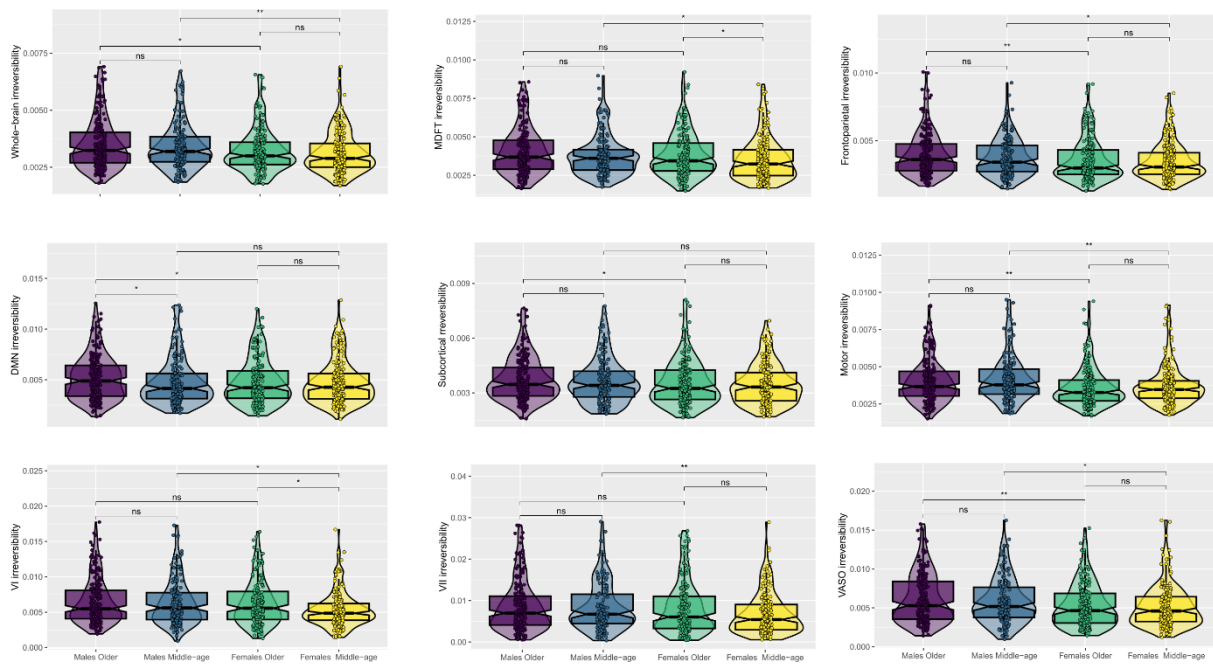


**Figure 1** Older males exhibit a higher degree of whole-brain temporal irreversibility compared to older females. Additionally, middle-aged males demonstrate a higher degree of irreversibility compared to middle-aged females. These results underscore the complex interplay between age, sex, and brain network organization. Within specific resting-state networks, the medial frontal network (MDFT), frontoparietal network, default mode network (DMN), subcortical network, motor network, visual networks (VI, VII), and visual association network (VASO), differences in temporal irreversibility among age and sex groups are evident, emphasizing age and sex-related variations in network dynamics.

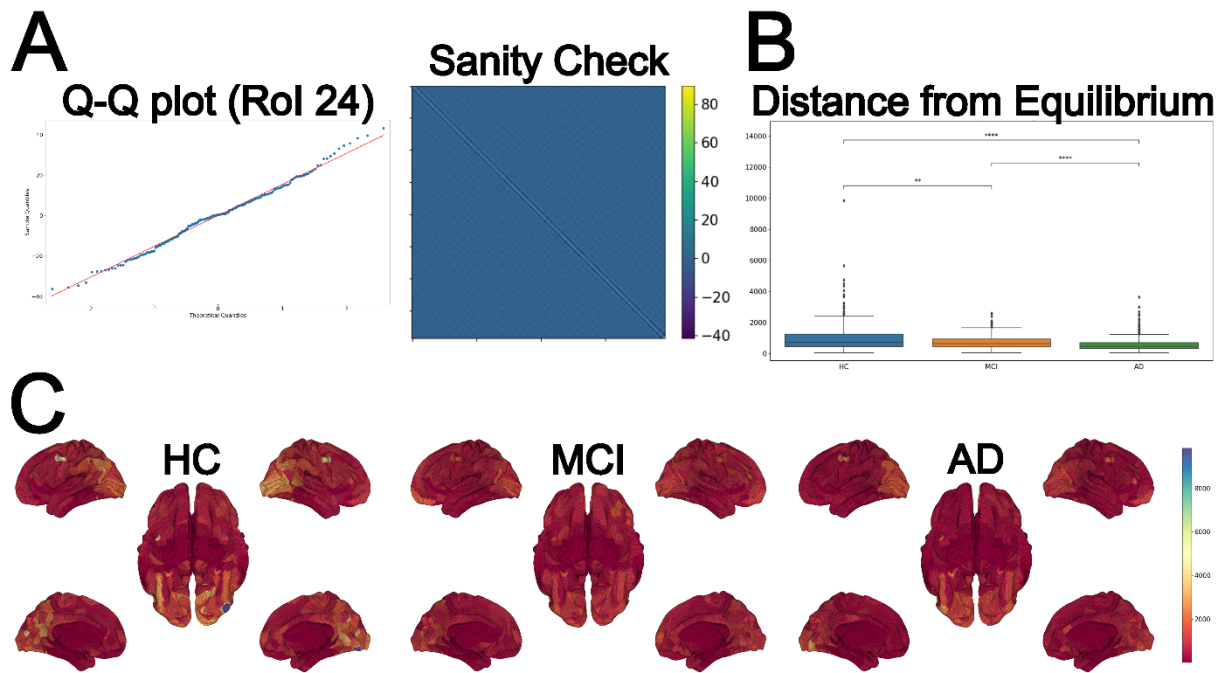


**Figure 2.** Deviation from equilibrium in Alzheimer's Disease. A). Required verifications for  $\eta(t)$ , where on the left, we can observe the Q-Q plot, a scatterplot created by plotting the quantiles of the derived noise against the standard normal distribution. B). Node-based deviation from equilibrium. Healthy controls showed higher deviations from equilibrium values across the whole-brain network than the MCI and AD stages. P-values are based on a two-sample t-tests, where \*\*\*\* represents  $p \leq 0.001$  and \*\*  $p \leq 0.01$ . C). Brain renders represent the deviation from equilibrium of the 379 areas for each disease stage. We can observe that the values are higher for the healthy control cohort and get lower and more homogeneous for subsequent stages of the disease.

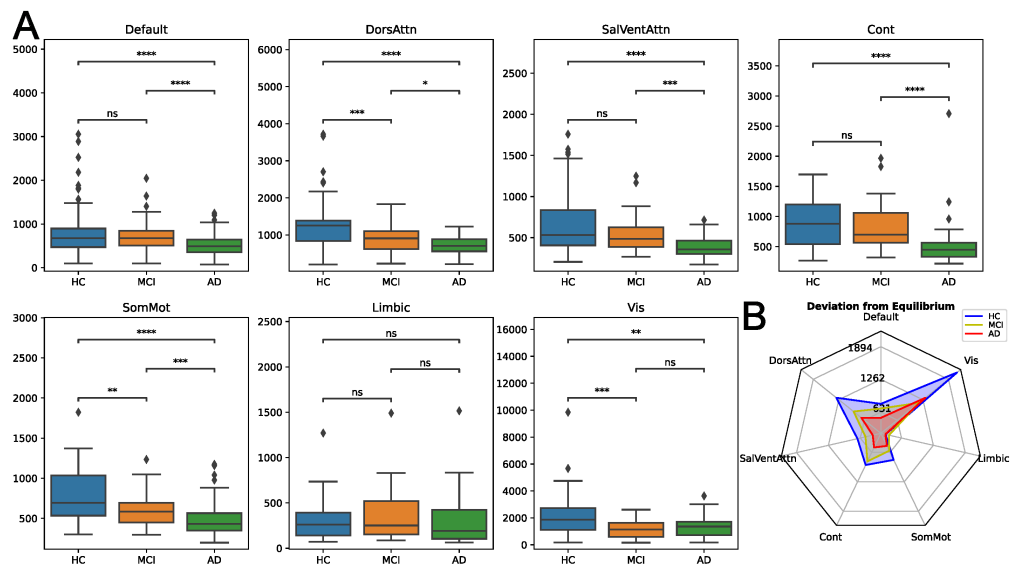


**Figure 3** Node-based deviation from equilibrium within resting-state networks. A) Compared to healthy control subjects, deviation from equilibrium was preserved for the limbic network at all stages. In contrast, it was preserved for DMN, salience, and control only between HC and MCI but significantly decreased for the MCI and AD stages for almost all networks. The visual network substantially reduced in the first stage of the disease but remained relatively unchanged for the later stages (i.e., AD). The dorsal attention and somatomotor networks are the ones that exhibit the most significant variations at all stages. B) The radar plot represents each stage's average deviation from equilibrium values per resting-state network.

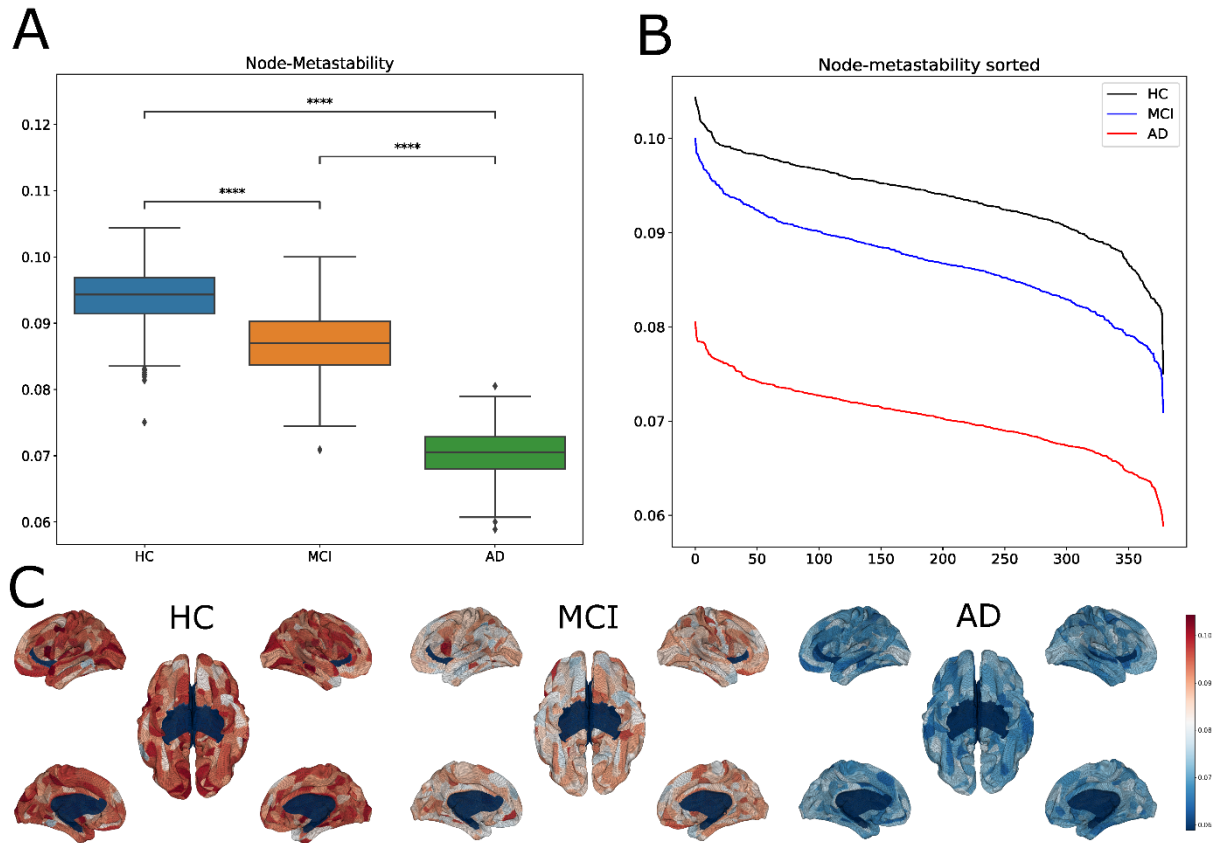


**Figure 4:** Dynamical complexity of Alzheimer's Disease stages. A). Node-metastability. Healthy controls showed higher node-metastability values across the whole-brain network than the MCI and AD stages. P-values are based on a two-sample t-test, where \*\*\*\* represents  $p \leq 0.001$ . B). Hierarchy. The red area marks the ten regions showing the highest metastability values in each stage. For the Healthy controls, brain areas showing the highest values were primarily located in the visual, somatomotor, and dorsal attention networks. For the MCI stage, the brain areas belonged to the same networks, except that, besides the visual network, with a lower metastability. Finally, during the AD stage, they were located again in the visual, somatomotor, and dorsal attention networks, although with a severe decrease in metastability. C). Brain renders represent each disease stage's metastability values of the 379 areas. The dynamical complexity of the healthy controls across the whole-brain networks is more complex than the dynamical complexity of the other two stages.

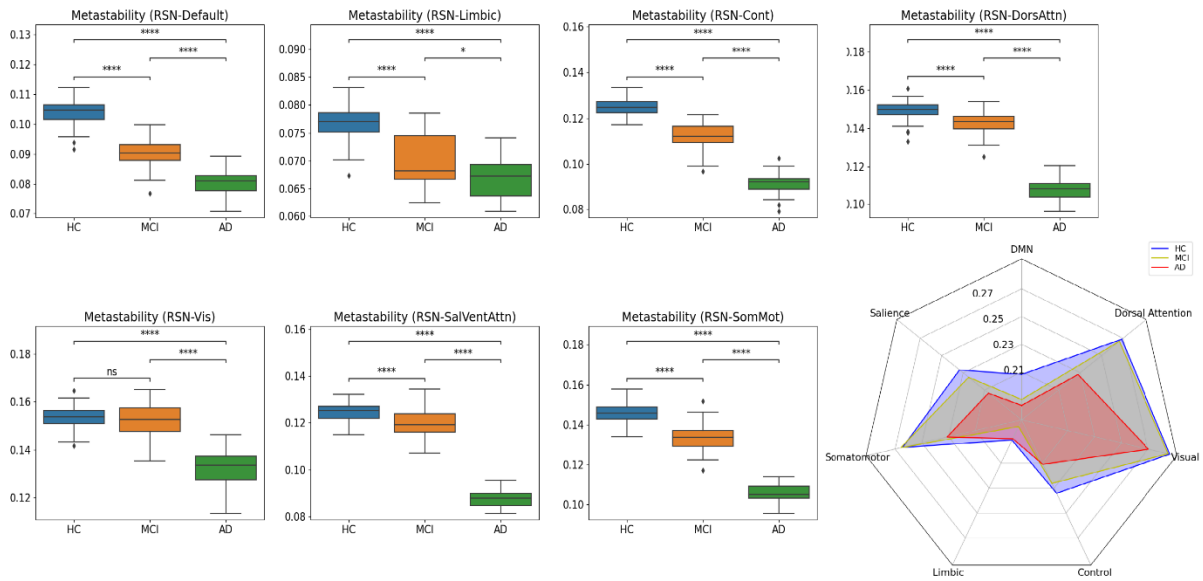
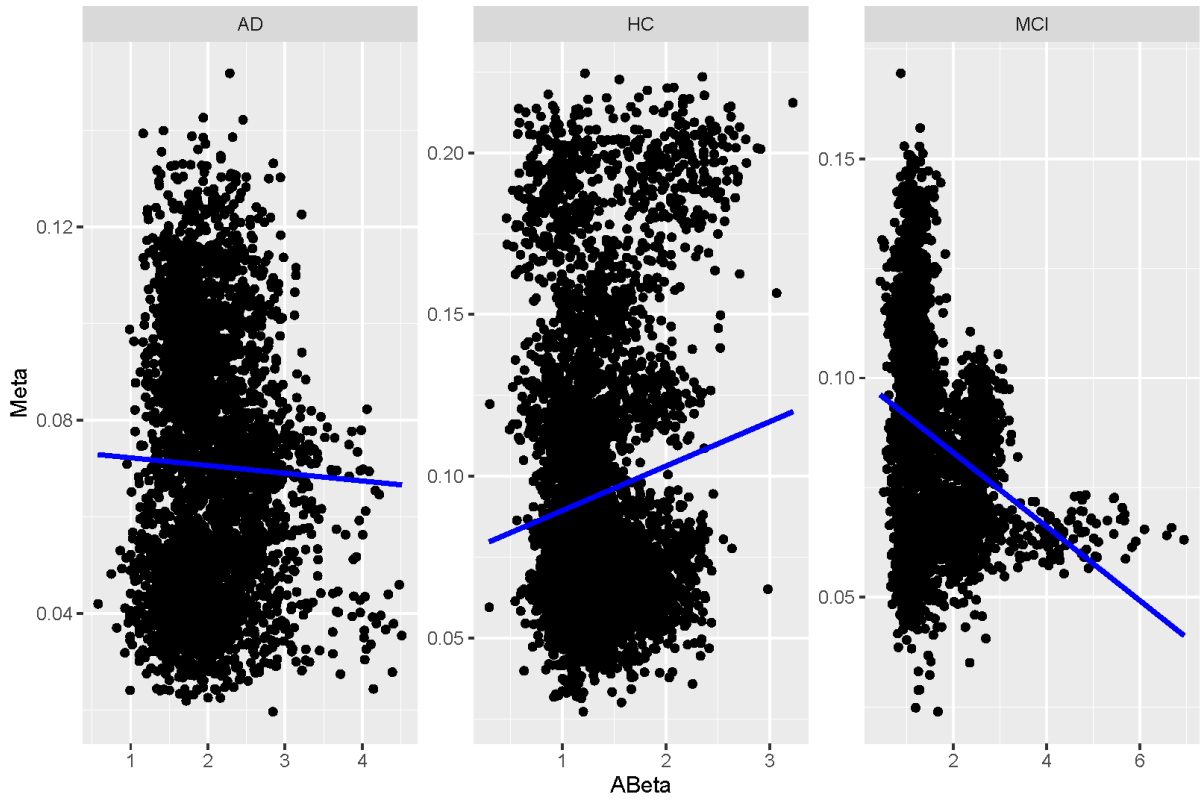


**Figure 5:** Node-metastability within resting state networks. A). Compared to healthy control subjects, node-metastability was preserved for the visual network between HC and MCI while significantly decreased in the MCI and AD stages for all the other networks. In general, although strongly affected, dorsal attention and somatomotor were the ones that more or less preserved their significance for their metastability. P-values are based on a two-sample t-test, where \* denotes  $p < 0.05$ , \*\*  $p < 0.01$ , and \*\*\* denotes  $p < 0.001$ . B). The radar plot represents each stage's average metastability values per resting state network.

Regression of Meta on ABeta by Cohort



Regression of Meta on Tau by Cohort

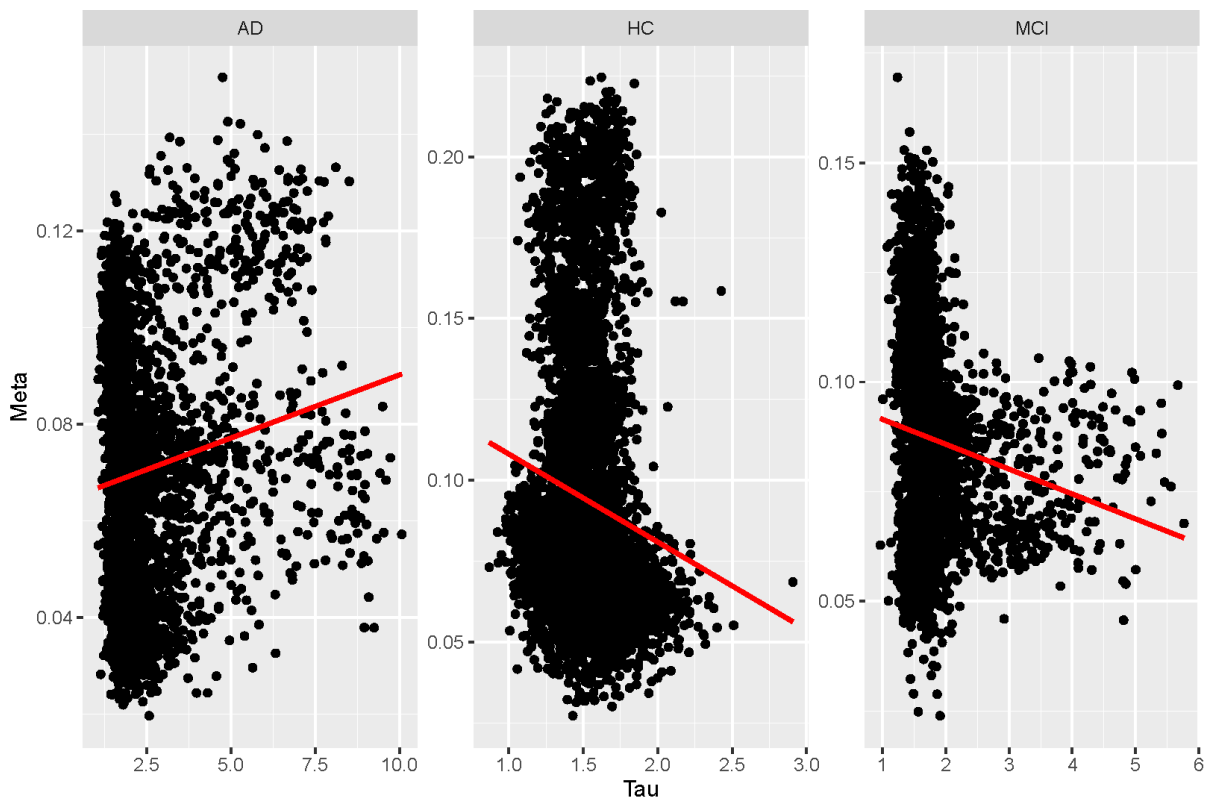
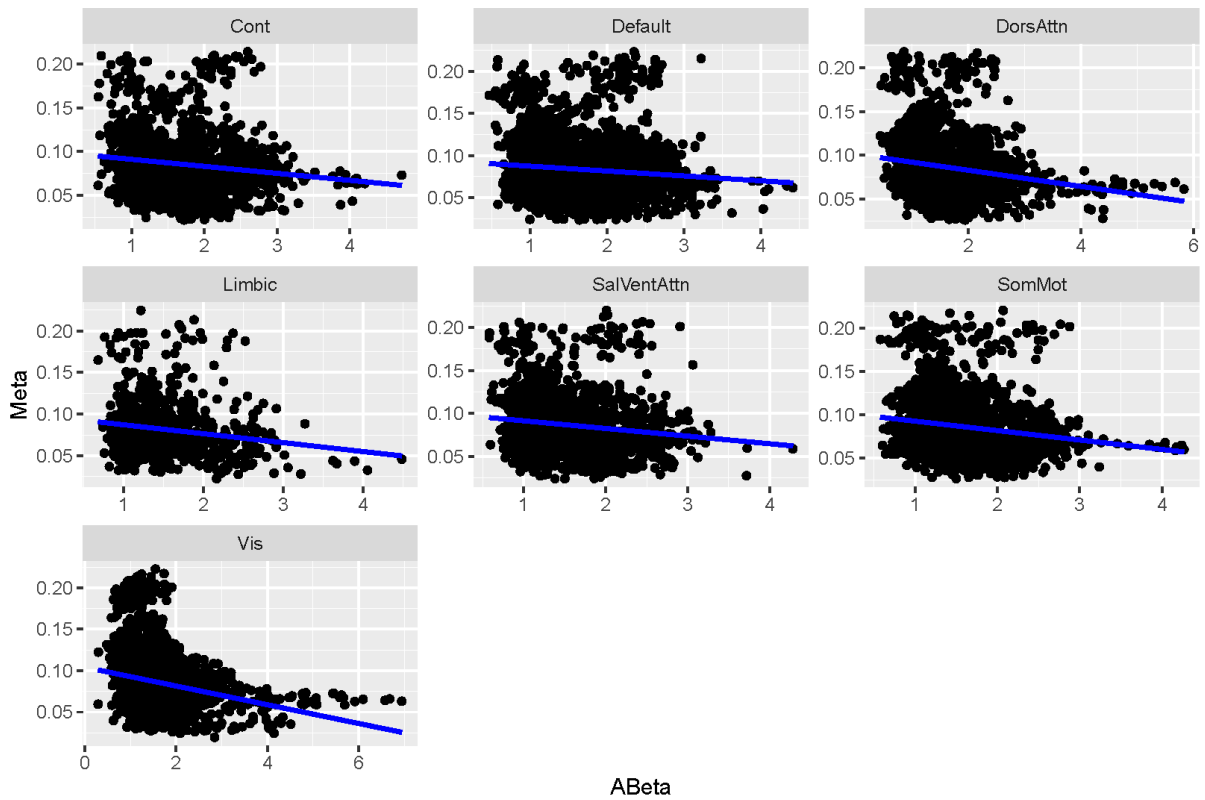
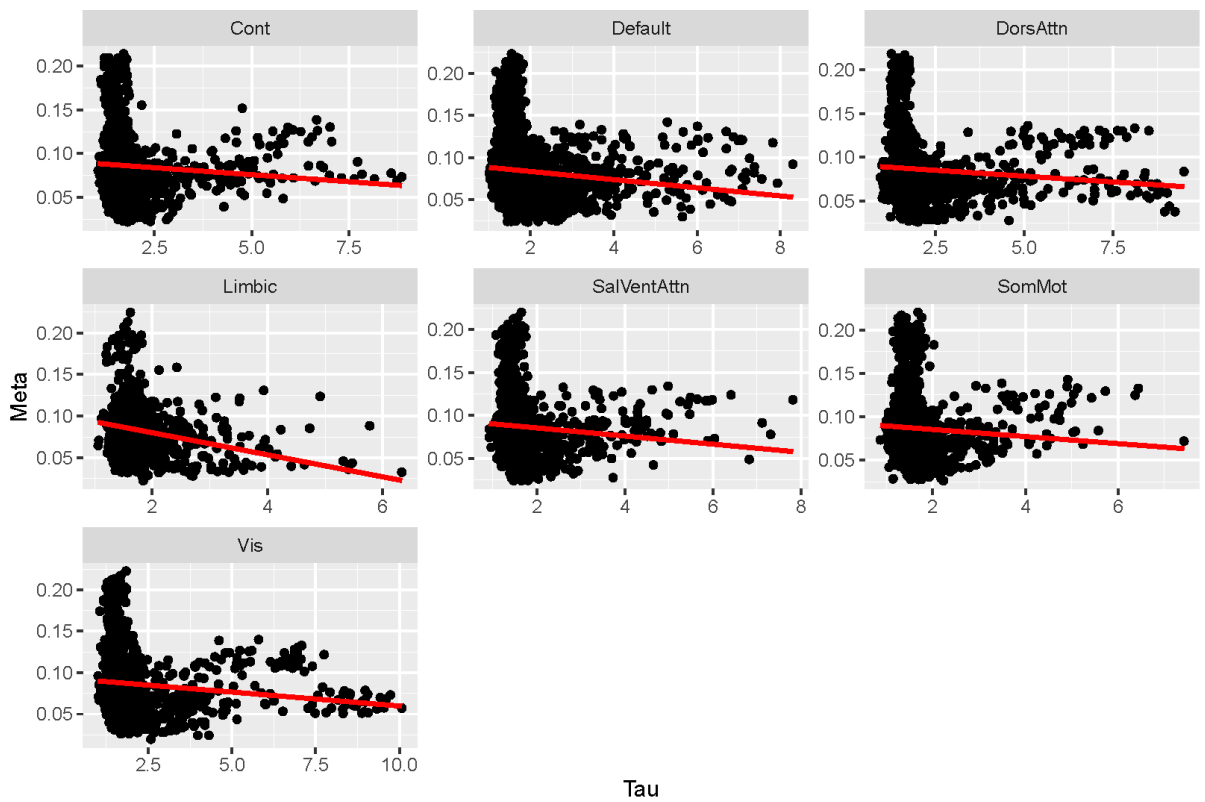


Figure 6. Multilevel models of the effects of ABeta and Tau on the whole brain

### Regression of Meta on ABeta by RSN



### Regression of Meta on Tau by RSN



**Figure 7:** Multilevel models of the effects of ABeta and Tau on resting-state networks.

	Overall sample	Middle-age group (< 65years)	Older group (≥ 65years)
Sample size, n (%)	702	331 (47.15)	371 (52.85)
Sex (female), n (%)	350 (49.86)	181 (54.68)	169 (45.55)
Age, mean (SD) [range]	65.98 (6.80) [50 – 80]	60.02 (3.84) [50 – 65]	71.30 (3.77) [66 – 80]

**Table 1:** Aging. Demographic characteristics of participants.

Diagnosis	n (fe- male)	Mean age	$\sigma$	Min. age	Max. age	Mean MMSE	$\sigma_{MMSE}$	Min. MMSE	Max. MMSE	Mean A $\beta$	Mean tau
HC	17 (10)	70.8	4.3	63.1	78.0	29.3	0.7	28	30	1.31	1.53
MCI	9 (3)	68.8	5.8	57.8	76.6	27.4	1.5	25	30	1.52	1.80
AD	10 (5)	72.0	9.6	55.9	86.1	21.3	6.8	9	30	2.01	2.46

**Table 2:** Alzheimer. Epidemiological information of the population

## 8. Bibliography

Deco, G., et al. 2022. The INSIDEOUT framework provides precise signatures of the balance of intrinsic and extrinsic dynamics in brain states. *Commun Biol* 5, 572.

G-Guzmán, E, et al. 2023. The lack of temporal brain dynamics asymmetry as a signature of impaired consciousness states." *Interface Focus* 13.3 (2023): 20220086.

Cruzat, Josephine, et al. 2023. Temporal irreversibility of large-scale brain dynamics in Alzheimer's disease." *Journal of Neuroscience* 43: 1643-1656.

Patow, G., et al. Direct observation of the deviation from equilibrium allows to characterize Alzheimer's Disease accurately (In prep).

Deco, G., et al. 2017. Novel Intrinsic Ignition Method Measuring Local-Global Integration Characterizes Wakefulness and Deep Sleep. *eneuro*, 4(5):ENEURO.0106–17.2017.

Puig, J., et al., 2020. The aging imageomics study: rationale, design, and baseline characteristics of the study population. *Mech Ageing Dev.* 189:111257.

Whitfield-Gabrieli S, Nieto-Castanon A. 2012. Conn: a functional connectivity toolbox for correlated and Anticorrelated brain networks. *Brain Connect.* 2:125–141.

Chao-Gan Y, Yu-Feng Z. 2010. DPARSF: a MATLAB toolbox for "pipeline" data analysis of resting-state fMRI. *Front Syst Neurosci.* 4:13.

Escrachs, A. et al., 2023. The effect of external stimulation on functional networks in the aging healthy human brain. *Cerebral Cortex* 33, 235–245

Stefanovski, L. et al., 2019. Linking molecular pathways and large-scale computational modeling to assess candidate disease mechanisms and pharmacodynamics in Alzheimer's disease." *Frontiers in computational neuroscience* 13 (2019): 54.

Triebkorn, P. et al., 2022. Brain simulation augments Machine-learning–based classification of dementia. *Alzheimer's & Dementia: Translational Research & Clinical Interventions*, 8(1).